Quantitative characterization of autofocusing and trapping of multi-Airy vortex beams

Liu Tan [ORCID],[1] Nana Liu,[1] Fuxi Lu,[1] Dongmei Liu [ORCID],[1] Beibei Yu [ORCID],[1] Yuting Li,[1] Hao Wu,[2] Kaijian Chen [ORCID],[1] Yizhe Chu,[1]
Peilong Hong [ORCID],[3,4,*] and Yi Liang [ORCID][1,5,†]

[1]*Guangxi Key Laboratory for Relativistic Astrophysics, Center on Nanoenergy Research, School of Physical Science and Technology, Guangxi University, Nanning, Guangxi 530004, China*

[2]*Department of Physics, Sichuan Normal University, Chengdu 610068, China*

[3]*School of Optoelectronic Science and Engineering, University of Electronic Science and Technology of China (UESTC), Chengdu 610054, China*

[4]*The MOE Key Laboratory of Weak-Light Nonlinear Photonics, TEDA Applied Physics Institute and School of Physics, Nankai University, Tianjin 300457, China*

[5]*State Key Laboratory of Featured Metal Materials and Life-cycle Safety for Composite Structures, Nanning 530004, China*

Abruptly autofocusing vortex beams were proposed for a variety of applications such as optical manipulation, but their quantitative characterization of their trapping capability remains largely unexplored. In this paper, we propose a type of autofocusing vortex beams named multi-Airy vortex beams (MAVBs) and investigate their autofocusing and trapping characteristics theoretically and experimentally. It is found that the autofocusing performance and trapping ability of MAVBs can be enhanced by adjusting the relevant parameters and increasing the number of superposed Airy within a certain range. Although the trapping force and trapping stiffness of MAVBs decrease as the topological charge increases, we found that MAVBs have advantages in capturing and manipulating large-sized particles in our experiments. In the process of manipulating multiple particles for rotation, the larger the topological charge, the more particles can be rotated simultaneously by MAVBs. Moreover, the speed and even the direction of rotation can be easily adjusted by controlling the degree of dispersion between particles. Our work provides a guide to quantitatively exploring the optical trapping capabilities of autofocusing vortex beams, which may lead to different photonic tools for optical trapping and manipulation.

I. INTRODUCTION

Since being first proposed in 1986 [1], optical tweezers (OTs) have been widely applied in various fields such as bioscience and chemistry [2–4]. Various types of OTs are being developed for more features or functionalities, for example, OTs based on structured light [4]. Structured light beams with customized phase, amplitude, and polarization exhibit unique properties, such as optical vortices carrying orbital angular momentum (OAM), which are highly desirable in optical manipulation. The optical vortex possesses a helical wave-front structure and acts as an "optical wrench" to rotate the particles in the OT system. Furthermore, it can form a dark spot in the beam center during its propagation [5], presenting a huge potential on reducing photodamage in biomedical applications of OTs [4,6]. Recently, a new kind of OT was proposed by introducing and implementing another special structured light called abruptly autofocusing beams (AAFBs) [7–9]. Without the help of a lens or nonlinearity, autofocusing beams can be automatically focused with a much strong focusing intensity, enabling manipulating particles at low power and reducing photodamage as well [10].

To improve the performance of autofocusing beams on optical manipulation and trapping, various abruptly autofocusing beams were induced with optical vortices [11–13] to form the so-called "dark beams" such as the circular Airy vortex beam (CAVB) [11,14,15], Airy Gaussian vortex beam [12,16–19], circular Pearcey vortex beam (CPVB) [20], and so on. These types of "dark beams" in OTs not only carry OAM to rotate particles, but also exhibit the possibility to reduce photodamage due to their dark optical traps. They are very valuable in optical manipulations and optical tweezers. Although previous work has demonstrated these beams can trap and manipulate particles, quantitatively characterizing their trapping force and stiffness and further optimizing their trapping performance lack detailed investigations [15,21,22].

In this paper, we propose a type of abruptly autofocusing "dark beams," called multi-Airy vortex beams (MAVBs), and quantitatively investigate the autofocusing performance and optical trapping capability of such beams in theory and experiment. Our results show that, with the same incident power, an increasing superimposed Airy number can enhance the autofocusing intensity and trapping performance of MAVBs, but increasing the topological charge number will generate a weaker autofocusing intensity and trapping force. However, increasing the topological charge number can help MAVBs to capture a larger object at the dark center of the beam, as demonstrated by the power spectra method in experiment. Our

*plhong@uestc.edu.cn
†liangyi@gxu.edu.cn

results present a quantitative understanding of the optical trapping capabilities of autofocusing vortex beams in theory and experiment, beneficial to different applications for optical manipulation and optical tweezers. For example, compared with conventional Guassian beams, OTs generated from MAVBs produce less photodamage when applied to biomedical research.

II. AUTOFOCUSING CHARACTERISTICS OF MAVBs

In the Cartesian coordinate system, a two-dimensional (2D) Airy beam at the initial plane can be defined as [7]

$$\varphi(x, y, z = 0) = \text{Ai}\left(\frac{x}{r_0}\right)\text{Ai}\left(\frac{y}{r_0}\right)\exp\left[\frac{\alpha}{r_0}(x + y)\right], \quad (1)$$

where r_0 is the arbitrary transverse scale factor, α is an exponential decay factor, and the Airy function $\text{Ai}(x) = \frac{1}{\pi}\int_0^\infty \cos(\frac{1}{3}t^3 + xt)dt$. Then, MAVBs can be generated by superposing 2D Airy beams with different azimuths and an optical vortex [13,14,23],

$$\psi(x, y, z = 0) = \sum_{j=1}^{N} \varphi_j(X_j, Y_j, z = 0)\left[\frac{-y + ix}{\sqrt{x^2 + y^2}}\right]^l, \quad (2)$$

$$\begin{bmatrix} X_j \\ Y_j \end{bmatrix} = \begin{bmatrix} \cos\left(2\pi\frac{j-1}{N}\right) & \sin\left(2\pi\frac{j-1}{N}\right) \\ -\sin\left(2\pi\frac{j-1}{N}\right) & \cos\left(2\pi\frac{j-1}{N}\right) \end{bmatrix}\begin{bmatrix} x \\ y \end{bmatrix} + \begin{bmatrix} c_0 \\ c_0 \end{bmatrix}, \quad (3)$$

where N represents the number of 2D Airy beams, φ_j represents the jth 2D Airy beams, (X_j, Y_j) are the position coordinates of the main lobes of the jth Airy beams on the x-y plane, c_0 is the transverse offset and l is the number of topological charges (TCs), and N is the number of superimposed beams. To explore the influence of the number of the superimposed beams and TCs, we first numerically simulate the propagation of MAVBs [24,25], where $\alpha = 0.04$, $r_0 = 50$ μm, $c_0 = 90$ μm. Then we further observe such propagation in the experimental setup of Fig. 1(a). The setup is similar to that of Ref. [23]. Finally, we quantitatively characterize the autofocusing characteristic of the MAVBs in the experiment.

A. Propagation of MAVBs with different superimposed Airy numbers

Here, we observed the autofocusing propagation of MAVBs with different superimposed beam numbers N. Figures 1(b) and 1(c) and Fig. 2(a) show the results of the cases with $N = 4$ [Figs. 1(b1)–1(b3)], $N = 8$ [Figs. 1(c1)–1(c3)], and $N = 12$ [Figs. 2(a1)–2(a3)] for comparison. Clearly, the initial and focal intensity distributions of these MAVBs can reveal their superposed beam number. All the MAVBs exhibit similar autofocusing behavior and have the same abruptly autofocusing positions. Due to the vortex which induces OAM, the autofocusing propagation of each MAVB goes with a transversal rotation (see Supplemental Videos 1–3 [26]), and a hollow pattern is easily formed in the center of the beam at the focal point. After autofocusing, beams diffract into their corresponding polygonal patterns which are emptier at the center. Notably, at the beginning ($z = 0$ mm), the peak intensity decreases with the increase of the superimposed beam number N [Figs. 1(b1), 1(c1), and 2(a1)]. Consequently, the autofocusing peak intensity of MAVB at the focal point
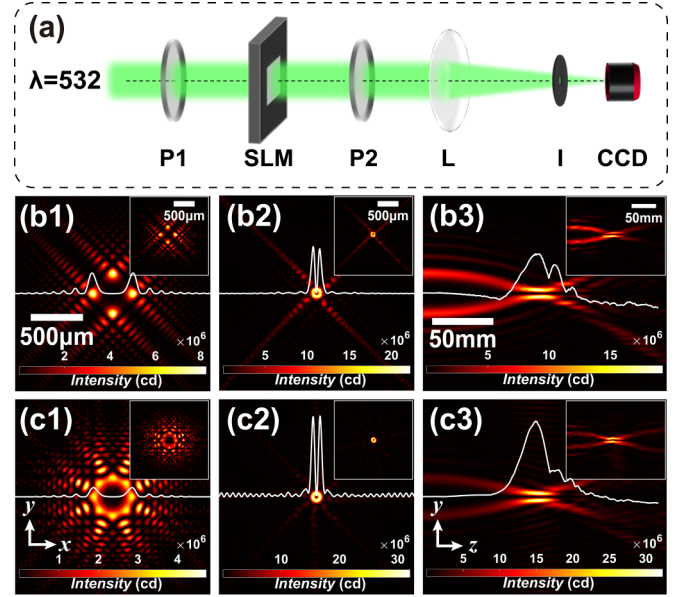

FIG. 1. Propagation of MAVBs ($l = 1$) with different superimposed Airy numbers N ($P = 1W$). (a) Experimental setup for generating MAVBs: P1 and P2, polarizers; SLM, spatial light modulator; L, lenses; I, irises; CCD, charge-coupled device. (b) $N = 4$; (c) $N = 8$. (b1) and (c1) and (b2) and (c2) are the intensity distributions of MAVBs ($l = 1, N = 4, 8$) in the initial position, and the focal positions $f = 98$ mm ($N = 4$) and 96 mm ($N = 8$), respectively. (b3) and (c3) are the side view. The white curve in the middle is the corresponding intensity distribution curve, and the illustration in the upper right corner shows the experimental results. The details of the transmission process can be viewed in Supplemental Videos 1–2 [26].

increases [Figs. 1(b2), 1(c2), and 2(a2)]. For example, here, when N is set from 4 to 12, the intensity is almost enhanced one time. Thus, a larger superimposed beam number N can enhance the peak intensity of the autofocusing ring. The simulation agrees well with the experiment, as shown in the insets of the figures.

B. Propagation of MAVBs with different topological charges

Next, we explored the effect of TCs (l) on the propagation of MAVBs. Figure 2 shows the intensity distribution of MAVBs ($N = 8$) with different TCs ($l = 1, 2, 3$) in the propagation process. As shown in Fig. 2 (see Supplemental Videos 3–5), the input intensity distributions of MAVBs with different TCs ($l = 1, 2, 3$) are the same [Figs. 2(a1)–2(c1)] but the intensity distributions at other positions are different. For instance, the central hollow area of the beams at the focal point becomes wider as a result of large l [Figs. 2(a2)–2(c2)]. Furthermore, the peak intensity at the focal point decreases significantly when l varies from 1 to 3. That is because large l causes the power of MAVB is more dispersed and power distributes at a large donut ring in the focal position. Thus, the corresponding autofocusing performance decreases [Figs. 2(a3)–2(c3)]. However, OAM of l empowers the beams with a rotating force, which is valuable for optical manipulation and especially benefits to optical trapping of big particles. Furthermore, large l not only can increase the rotation speed
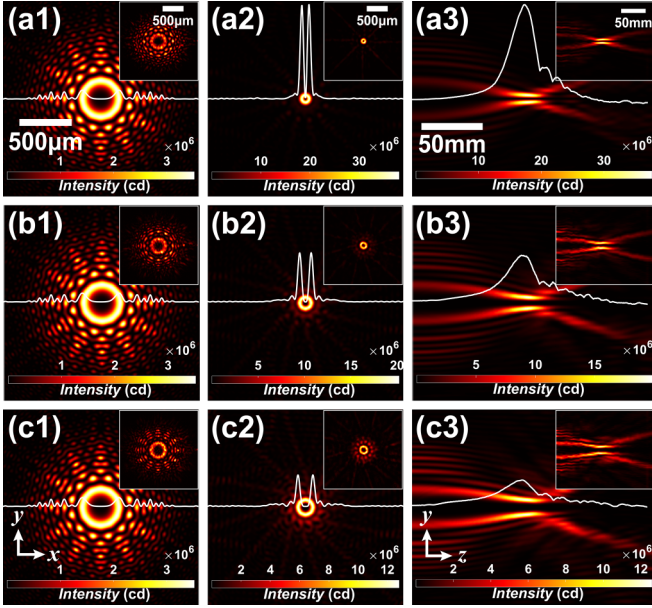
FIG. 2. Propagation of MAVBs ($N = 12$) with different TCs. (a) $l = 1$; (b) $l = 2$; (c) $l = 3$. (a1)–(c1) and (a2)–(c2) are the intensity distribution of MAVBs ($N = 12$, $l = 1, 2, 3$) in the initial position, and the focal positions $f = 96$ mm ($l = 1$), 95 mm ($l = 2$), 94 mm ($l = 3$), respectively. (a3)–(c3) are the side view. The white curve in the middle is the corresponding intensity distribution curve, and the illustration in the upper right corner shows the experimental results. The details of the transmission process can be viewed in Supplemental Videos 3–5 [26].

but also slightly reduce the autofocusing length [$z = f = 96$ mm ($l = 1$), 95 mm ($l = 2$), 94 mm ($l = 3$)]. The corresponding MAVB with a much large l can reach its focal point more quickly. The above phenomena are also demonstrated in the experiment, as shown in the insets of Fig. 2.

C. Quantitative analysis of autofocusing on performance of MAVBs

To quantitatively analyze the autofocusing performance of MAVBs with different parameters (N, l, α, r_0, c_0), here, an autofocusing coefficient K ($K = I_{max}/I_0$) is defined to represent the ratio between the maximum light intensity (I_{max}) at the focal plane and the maximum light intensity (I_0) at the initial plane. A large K indicates a better autofocusing performance.

First, the changes of the autofocusing coefficient K with N under different TCs is presented in Fig. 3(a). Obviously, increasing N can enhance autofocusing performance because large N causes a weaker initial intensity peak and stronger focal intensity under the same incident power. However, when N increase to a certain value, the autofocusing coefficient K reaches a maximum and the enhancement of autofocusing performance stops. Here, after N reaches 12, the K of MAVBs with different TCs are unchanged at 44.92 ($l = 0$), 10.87 ($l = 1$), 5.75 ($l = 2$), and 3.65 ($l = 3$). Moreover, from Fig. 2, one can know the initial intensity is the same for all TCs (l) while the intensity peak in the focal point decreases with a large l. Thus, increasing l will weaken the autofocusing performance
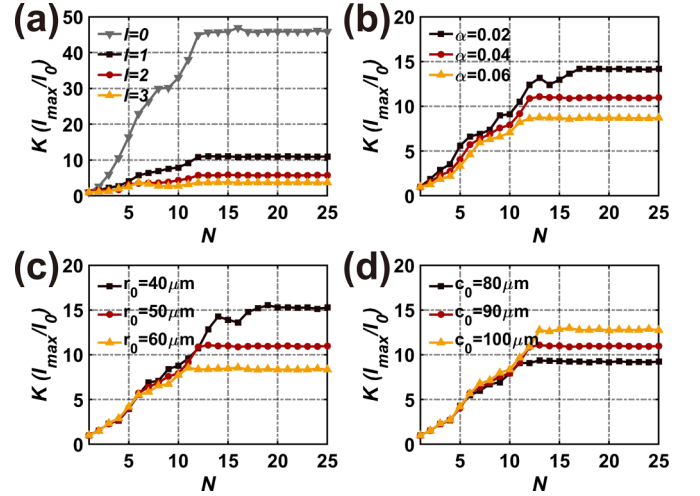

FIG. 3. Autofocusing performance of MAVBs ($N = 12$) with different parameters. (a)–(d) are the changes of autofocusing coefficient $K(I_{max}/I_0)$ corresponding to N of MAVBs with different TCs ($l = 0, 1, 2, 3$), exponential decay factor ($\alpha = 0.02, 0.04, 0.06$), arbitrary transverse scale factor ($r_0 = 40, 50, 60$ μm), and transverse offset ($c_0 = 80, 90, 100$ μm), respectively.

of MAVBs, as shown in Fig. 3(a). Figures 3(b)–3(d) are the simulation results of the K varying with N under different α, r_0, c_0, respectively. The autofocusing performance of MAVBs is weakened when α and r_0 increase, while the effect of c_0 is the opposite. Different from the influence of l on MAVBs [Fig. 3(a)], the differences between the autofocusing coefficients K of MAVBs under different α, r_0, or c_0 are little when N is small [Figs. 3(b) and 3(c)]. However, these three parameters significantly affect the autofocusing coefficient maximum when N is large. The autofocusing coefficient maximum goes up with smaller α, r_0, and larger c_0.

III. POWER FLOW OF THE 2D MAVBs

The Poynting vector $\vec{S}$ represents the electromagnetic energy per unit area per unit time that passes perpendicular to the direction of the energy transfer ($\vec{S} = \vec{E} \times \vec{H}$), and its direction is the direction of the electromagnetic energy transfer. To better understand the above propagation phenomena of MAVBs, we simulated the evolution of its transverse Poynting vector $\vec{S}_\perp$ with propagation. At the same time, the transverse Poynting vector also reflects the transverse scattering force
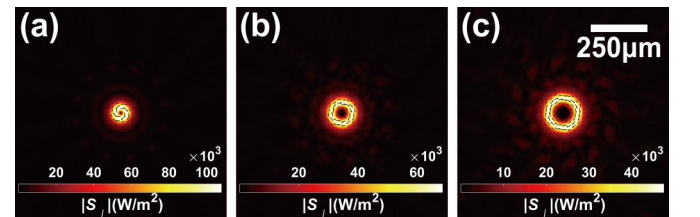

FIG. 4. The transversal power flow of MAVBs ($N = 12$) in the focal position, where the black arrows represent the direction of energy flow. (a) $l = 1$; (b) $l = 2$; (c) $l = 3$. See Videos 6–8 in the Supplemental Material [26].
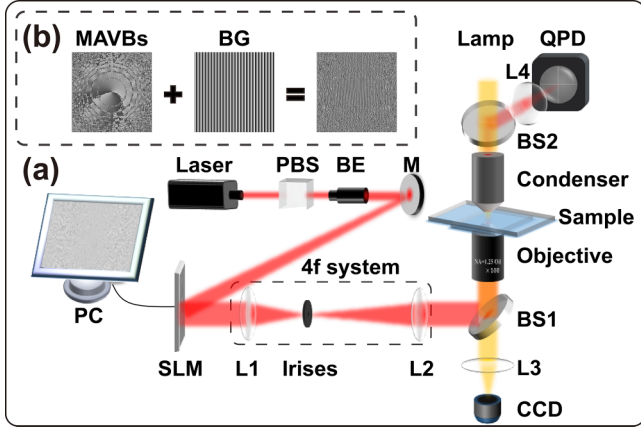
FIG. 5. (a) Experimental setup for trapping and manipulating particles. Laser, λ = 1064 nm; PBS, polarizing beam splitter; BE, beam expanders; M, mirror; SLM, spatial light modulator; L, lenses; BS, beam splitter; CCD, charge-coupled device; Objective, oil objective [numerical aperture (NA) = 1.25, ×100]; QPD, quadrant photoelectric detectors. (b) Phase image of MAVBs. BG, blazed grating.

on the Rayleigh particle [2]. Usually, the transversal Poynting vector $\vec{S}_\perp$ can be expressed as [5]

$$\vec{S}_\perp = \frac{i}{4\eta_0 k}[\psi \nabla_\perp \psi^* - \psi^* \nabla_\perp \psi], \qquad (4)$$

where $\eta_0 = \sqrt{\mu_0/\varepsilon_0}$ is the impedance of free space, $\nabla_\perp = \frac{\partial}{\partial x}\vec{e}_x + \frac{\partial}{\partial y}\vec{e}_y$, and $k = 2\pi/\lambda$ is the wave vector.

Figure 4 shows the distribution of the transverse Poynting vector at the focal plane, and the black arrows in the figure represent the direction of energy flow. At the beginning of the video (Supplemental Videos 6–8 [26]), the transverse Poynting vector gradually converges to the center in a spiral way, and reaches its maximum value at the focal point. At this point, the energy flows neither inward nor outward, but along the tangent direction of the surrounding hole. Therefore, we can speculate that the small particles captured by the MAVBs will rotate around the hole. After the focus, the energy diffuses outward quickly. For power flow, the direction of the arrow is related to the positive or negative of the TCs. Here, we only discuss the case of $l > 0$, corresponding to a clockwise direction of power flow. Since the size of the focal ring increases as the increase of topological charges, the Poynting vector of MAVBs generally decreases with increasing TCs.

IV. TRAPPING FORCE CHARACTERISTICS OF MAVBs

To further demonstrate the benefits of using MAVBs in particle manipulation, we constructed a holographic optical tweezers platform based on MAVBs, as illustrated in Fig. 5(a). The optical trapping force's magnitude is generally proportional to the particle's position deviation from the optical trap's center, making the scaling factor (referred to as the optical trapping stiffness κ_r) a crucial parameter for characterizing the beam trapping performance. In our experiments, the particle's position information within the optical trap was recorded using a quadrant photodetector (QPD). Subsequently, we obtained the optical trapping stiffness κ_r by processing the data using the power spectrum method [2,27]. Additionally, we generated a hologram in conjunction with the blazed grating
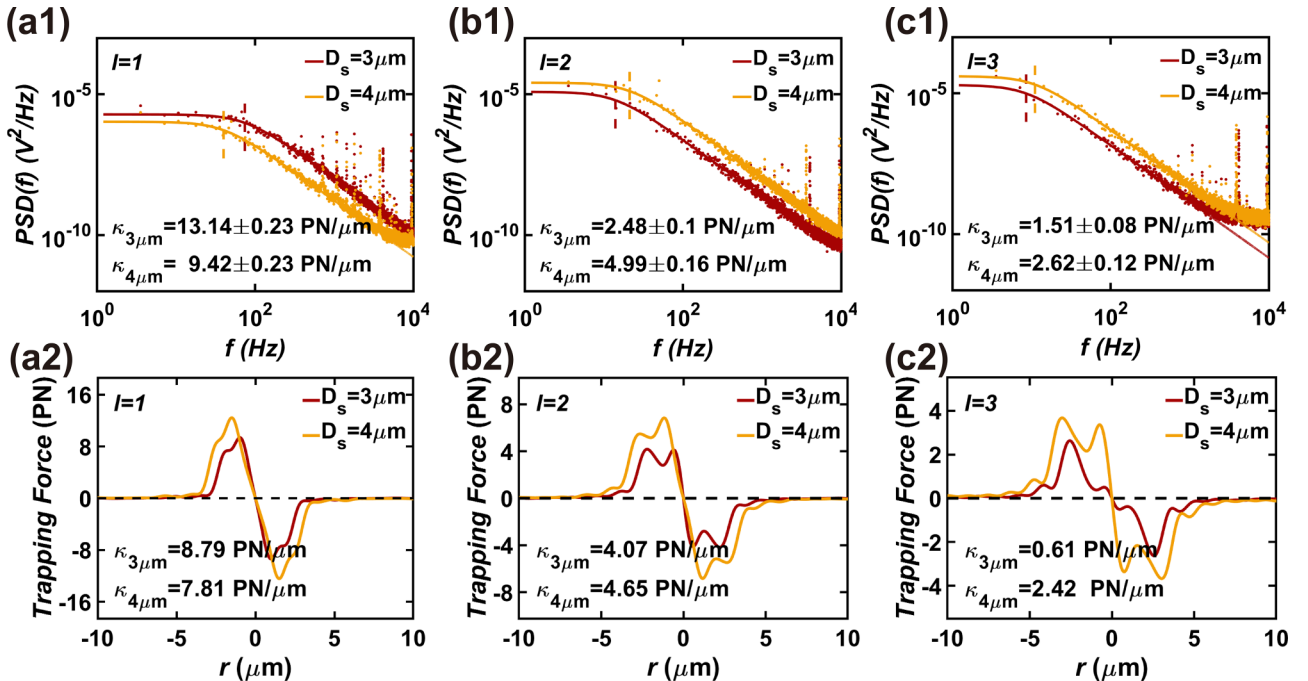

FIG. 6. The ability of MAVBs to capture single PS microparticles. (a1)–(c1) Experiment: Power spectral density (PSD) maps of single PS (3 μm red; 4 μm yellow) captured by MAVBs with different topological charges ($l = 1, 2, 3$) at a power of $P = 32$ mW. The dashed lines indicate the position of the f_c, and the trapping stiffness κ_r ($\kappa_r = f_c * 2\pi\gamma$) is shown in the lower left-hand corner. (a2)–(c2) Simulation: The trapping force distribution of MAVBs. The bottom left panel displays the corresponding trapping stiffness κ_r ($\kappa_r = dF/dr$).
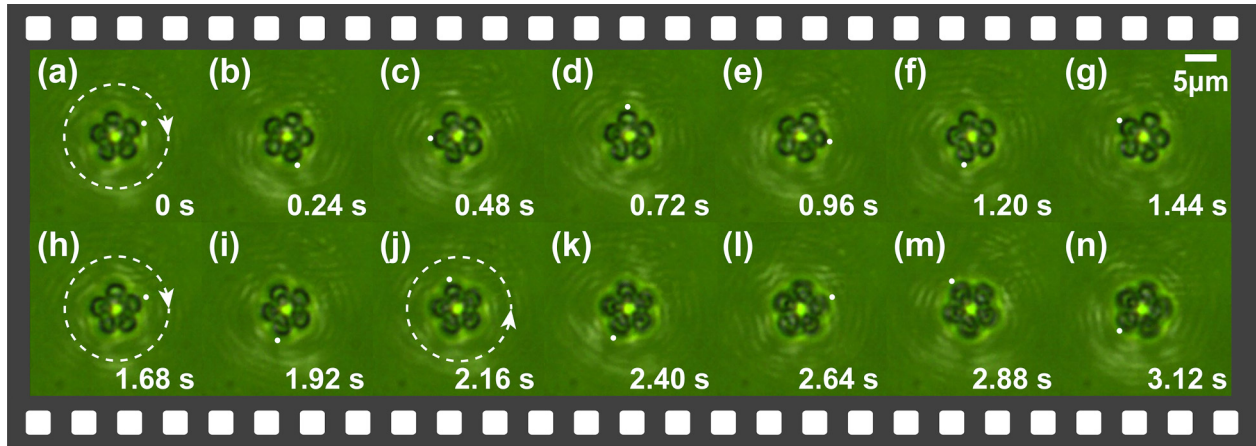
FIG. 7. MAVBs ($N = 12$, $l = 1$) rotate multiple PS ($D_s = 1.5$ μm) particles. (a)–(g) MAVBs manipulate five PS particles to rotate along the clockwise direction. (h)–(n) After adjusting the degree of dispersion between particles, the direction of the rotation of particles changes from clockwise to counterclockwise. See Videos 12–14 in the Supplemental Material [26].

[as shown in Fig. 5(b)], which helped enhance the capture power to some extent.

A. Trapping force of MAVBs

Figures 6(a1)–6(c1) display the power spectral density (PSD) of MAVBs ($N = 12$, $l = 1, 2, 3$) capturing a single polystyrene particle (PS) ($P = 32$ mW). Based on the Langevin equation, the corner frequency f_c is defined as $f_c = \kappa_r/2\pi\gamma$, where γ is the particle friction coefficient ($\gamma = 3\pi\eta D_s$, where η is the viscosity of the solution, and D_s is the diameter of the particle). The red and yellow lines indicate the trapped particle diameters of 3 and 4 μm, respectively, and the dashed lines represent the position of the corner frequency f_c. In Mie regime, the calculation of optical forces can be based on various approaches such as the generalized Lorentz-meter theory and Cartesian multipole expansion theory [28,29]. Here, we simulated the trapping force of MAVBs using the full-wave generalized Lorentz-meter theory and the Maxwell stress tensor technique [30], as shown in Figs. 6(a2)–6(c2).

Through analyzing both the experimental and simulation results, we found that increasing the topological charge reduces the trapping force and stiffness of MAVBs near the focal point due to the dispersion of energy. However, when comparing Fig. 6(a) and Fig. S1 [26], we noticed that MAVBs ($N = 12$, $l = 1$) exhibit greater trapping stiffness than MABs ($N = 12$), even though the energy of the latter is more concentrated at the focus [Fig. 3(a)]. This suggests that MAVBs are more stable and advantageous in capturing larger particles. Two scenarios must be considered when exploring the variation of trapping force and trapping stiffness with particle size. If the particle's size is bigger than the trap ring, the gradient force will drive the particle to the beam center. The trapping force increases with increasing particle size, while the trapping stiffness decreases, as shown in Figs. 6(a1) and 6(a2). When the particle size is smaller than the trap ring, the particle will be trapped on one side of the trap ring [31]. As the scattering surface increases with the particle size, the trapping force and trapping stiffness also increase, as depicted in Figs. 6(b1) and 6(b2) and Figs. 6(c1) and 6(c2). The diameters of the trap

rings of MAVBs at the focus are approximately 2 μm ($l = 1$), 3 μm ($l = 2$), and 4 μm ($l = 3$). Moreover, considering the important role of environmental damping forces in optical vortex trapping, only particles with sufficient damping will be stably trapped, otherwise they will undergo periodic or nonperiodic orbital motions [32,33].

B. MAVBs rotate microparticles

MAVBs, being carriers of OAM, offer an additional degree of freedom to manipulate particle rotation. Supplemental Videos 9–11 [26] demonstrate that MAVBs ($N = 12$, $l = 1$) can control the rotation of single polystyrene particles (PSs) as long as the capture ring size is larger than the particle size. Figure 7 shows the process by which MAVBs ($N = 12$, $l = 1$) manipulate the rotation of multiple PS particles ($D_s = 1.5$ μm). In Figs. 7(a)–7(g), the direction of particle rotation is consistent with the direction of the transverse Poynting vector in Fig. 4. The frequent collisions between particles allow them to transfer OAM, which overcomes the rotation difficulties caused by the intensity inhomogeneity [34]. Therefore, the speed of particle rotation can be experimentally regulated by manipulating the degree of dispersion between particles. MAVBs with larger topological charges can manipulate larger and more numerous particles simultaneously.

In multiparticle systems, the particles sometimes exhibit rotational orbital motion in the opposite direction of the incident helicity, known as negative optical torque. Previous studies have shown that the negative optical torque phenomenon often appears in multiparticle arrays under the effect of discrete rotational symmetry and phase delay [35,36]. The number and size of particles, as well as their arrangement, can affect the appearance of negative optical torque [35–38]. The degree of dispersion between particles can be adjusted in the experiment to observe the phenomenon of positive and negative torque crossing. Figures 7(h)–7(n) show the process of changing the direction of particle rotation from clockwise [positive optical torque (POT)] to counterclockwise [negative optical torque (NOT)] by reducing the degree of dispersion between particles. The emergence of negative optical torque

further expands the range of applications of MAVBs in microparticle manipulation.

V. CONCLUSION

In this paper, we have investigated the self-focusing propagation dynamics and quantitative capture properties of MAVBs both theoretically and experimentally. Our findings reveal that the autofocusing performance of MAVBs can be improved by increasing the number of superimposed beams N or decreasing the number of topological charges l. However, we observed that when N is large, the maximum self-focusing coefficient K of MAVBs does not significantly change. At this stage, the self-focusing performance of MAVBs is mainly influenced by the other three parameters (α, r_0, c_0). Specifically, we found that the effect of c_0 is positive, while the effect of r_0 and α is negative.

Our investigation of the trapping force characteristics of MAVBs reveals that the trapping stiffness of MAVBs decreases with the increase of topological charge when trapping a single particle, and their trapping force increases with the

increase of particle size. Our experimental results demonstrate that MAVBs have advantages in capturing large-sized particles. Furthermore, we observed that by tuning the discrete degree of particles, not only can the rotation speed be adjusted, but also the positive and negative torque crossover can be observed in the experiment. Overall, our findings open up the possibility of developing optical manipulation tools based on abruptly autofocusing vortex beams for various biomedical applications, such as accessing the deformability of cells and reducing photodamage on biological samples, as has been previously demonstrated by other researchers [2,3,39].

[1] A. Ashkin, J. M. Dziedzic, J. E. Bjorkholm, and S. Chu, Observation of a single-beam gradient force optical trap for dielectric particles, Opt. Lett. **11**, 288 (1986).

[2] P. Jones, O. Maragó, G. Volpe, P. Jones, O. Marago, and G. Volpe, *Optical Tweezers: Principles & Applications* (Cambridge University Press, 2015).

[3] A. I. Bunea and J. Gluckstad, Strategies for optical trapping in biological samples: Aiming at microrobotic surgeons, Laser Photonics Rev. **13**, 1800227 (2019).

[4] Y. J. Yang, Y. X. Ren, M. Z. Chen, Y. Arita, and C. Rosales-Guzman, Optical trapping with structured light: A review, Adv. Photonics **3**, 034001 (2021).

[5] L. Allen, M. W. Beijersbergen, R. J. Spreeuw, and J. P. Woerdman, Orbital angular momentum of light and the transformation of Laguerre-Gaussian laser modes, Phys. Rev. A **45**, 8185 (1992).

[6] H. Rubinsztein-Dunlop, A. Forbes, M. V. Berry, M. R. Dennis, D. L. Andrews, M. Mansuripur, C. Denz, C. Alpmann, P. Banzer, T. Bauer, E. Karimi, L. Marrucci, M. Padgett, M. Ritsch-Marte, N. M. Litchinitser, N. P. Bigelow, C. Rosales-Guzman, A. Belmonte, J. P. Torres, T. W. Neely *et al.*, Roadmap on structured light, J. Opt. **19**, 013001 (2017).

[7] N. K. Efremidis and D. N. Christodoulides, Abruptly autofocusing waves, Opt. Lett. **35**, 4045 (2010).

[8] D. G. Papazoglou, N. K. Efremidis, D. N. Christodoulides, and S. Tzortzakis, Observation of abruptly autofocusing waves, Opt. Lett. **36**, 1842 (2011).

[9] P. Zhang, J. Prakash, Z. Zhang, M. S. Mills, N. K. Efremidis, D. N. Christodoulides, and Z. Chen, Trapping and guiding microparticles with morphing autofocusing Airy beams, Opt. Lett. **36**, 2883 (2011).

[10] F. X. Lu, H. Wu, Y. Liang, L. Tan, Z. F. Tan, X. Feng, Y. Hu, Y. X. Xiang, X. B. Hu, Z. G. Chen, and J. J. Xu, Bessel-modulated autofocusing beams for optimal trapping implementation, Phys. Rev. A **104**, 043524 (2021).

[11] Y. Jiang, S. Zhao, W. Yu, and X. Zhu, Abruptly autofocusing property of circular Airy vortex beams with different initial launch angles, J. Opt. Soc. Am. A **35**, 890 (2018).

[12] B. Chen, C. Chen, X. Peng, Y. Peng, M. Zhou, and D. Deng, Propagation of sharply autofocused ring Airy Gaussian vortex beams, Opt. Express **23**, 19288 (2015).

[13] Y. Jiang, K. Huang, and X. Lu, Propagation dynamics of abruptly autofocusing Airy beams with optical vortices, Opt. Express **20**, 18579 (2012).

[14] Y. K. Chen, X. W. Lin, S. Y. Lin, S. Y. Mo, L. Y. Wan, and Y. Liang, Propagation dynamics of deformed 2D vortex Airy beams, Chin. Opt. Lett. **15**, 080801 (2017).

[15] M. S. Chen, S. J. Huang, X. P. Liu, Y. Chen, and W. Shao, Optical trapping and rotating of micro-particles using the circular Airy vortex beams, Appl. Phys. B **125**, 184 (2019).

[16] K. L. Guo, J. T. Xie, G. X. Chen, Y. Wu, Y. Q. Liang, S. H. Hong, F. Ye, J. B. Zhang, and D. M. Deng, Abruptly autofocusing properties of the chirped circular Airy Gaussian vortex beams, Opt. Commun. **477**, 126369 (2020).

[17] J. L. Zhuang, L. P. Zhang, and D. M. Deng, Tight-focusing properties of linearly polarized circular Airy Gaussian vortex beam, Opt. Lett. **45**, 296 (2020).

[18] Z. Pang and D. Deng, Propagation properties and radiation forces of the Airy Gaussian vortex beams in a harmonic potential, Opt. Express **25**, 13635 (2017).

[19] S. He, B. A. Malomed, D. Mihalache, X. Peng, X. Yu, Y. He, and D. Deng, Propagation dynamics of abruptly autofocusing circular Airy Gaussian vortex beams in the fractional Schrödinger equation, Chaos Solitons Fractals **142**, 110470 (2021).

[20] C. Sun, D. Deng, G. Wang, X. Yang, and W. Hong, Abruptly autofocusing properties of radially polarized circle Pearcey vortex beams, Opt. Commun. **457**, 124690 (2020).

[21] Y. Jiang, K. Huang, and X. Lu, Radiation force of abruptly autofocusing Airy beams on a Rayleigh particle, Opt. Express **21**, 24413 (2013).

[22] W. L. Lu, X. Sun, H. J. Chen, S. Y. Liu, and Z. F. Lin, Abruptly autofocusing property and optical manipulation of circular Airy beams, Phys. Rev. A **99**, 013817 (2019).

[23] F. X. Lu, L. Tan, Z. F. Tan, H. H. Wu, and Y. Liang, Dynamical power flow and trapping-force properties of two-dimensional airy-beam superpositions, Phys. Rev. A **104**, 023526 (2021).

[24] F. L. Wang and Y. Liang, Split autofocusing Pearcey beams with flexible trapping capabilities, Opt. Commun. **484**, 126681 (2021).

[25] J. Van Roey, J. van der Donk, and P. E. Lagasse, Beam-propagation method: Analysis and assessment, J. Opt. Soc. Am. **71**, 803 (1981).

[26] See Supplemental Material at http://link.aps.org/supplemental/10.1103/PhysRevA.107.043501 for details on the propagation of MAVBs, dynamical flow evolution, and manipulation of particle rotation.

[27] K. Berg-Sørensen and H. Flyvbjerg, Power spectrum analysis for optical tweezers, Rev. Sci. Instrum. **75**, 594 (2004).

[28] Y. K. Jiang, J. Chen, J. Ng, and Z. F. Lin, Decomposition of optical force into conservative and nonconservative components, arXiv:1604.05138 (2016).

[29] J. Du, C.-H. Yuen, X. Li, K. Ding, G. Du, Z. Lin, C. T. Chan, and J. Ng, Tailoring optical gradient force and optical scattering and absorption force, Sci. Rep. **7**, 18042 (2017).

[30] H. Wu, X. Zhang, P. Zhang, P. Jia, Z. Wang, Y. Hu, Z. Chen, and J. Xu, Optical pulling force arising from non-

[31] paraxial accelerating beams, Phys. Rev. A **103**, 053511 (2021).

[31] N. B. Simpson, K. Dholakia, L. Allen, and M. J. Padgett, Mechanical equivalence of spin and orbital angular momentum of light: An optical spanner, Opt. Lett. **22**, 52 (1997).

[32] J. Ng, Z. Lin, and C. T. Chan, Theory of Optical Trapping by an Optical Vortex Beam, Phys. Rev. Lett. **104**, 103601 (2010).

[33] A. Karnieli, S. Tsesses, G. Bartal, and A. Arie, Emulating spin transport with nonlinear optics, from high-order skyrmions to the topological Hall effect, Nat. Commun. **12**, 1092 (2021).

[34] B. Gao, J. Wen, G. Zhu, L. Ye, and L. G. Wang, Precise measurement of trapping and manipulation properties of focused fractional vortex beams, Nanoscale **14**, 3123 (2022).

[35] J. Chen, J. Ng, K. Ding, K. H. Fung, Z. Lin, and C. T. Chan, Negative optical torque, Sci. Rep. **4**, 6386 (2014).

[36] F. Han, J. A. Parker, Y. Yifat, C. Peterson, S. K. Gray, N. F. Scherer, and Z. Yan, Crossover from positive to negative optical torque in mesoscale optical matter, Nat. Commun. **9**, 4897 (2018).

[37] N. Sule, Y. Yifat, S. K. Gray, and N. F. Scherer, Rotation and negative torque in electrodynamically bound nanoparticle dimers, Nano Lett. **17**, 6548 (2017).

[38] T. Qi, F. Han, W. Liu, and Z. Yan, Stable negative optical torque in optically bound nanoparticle dimers, Nano Lett. **22**, 8482 (2022).

[39] Y. Liang, G. Liang, Y. Xiang, J. Lamstein, R. Gautam, A. Bezryadina, and Z. Chen, Manipulation and Assessment of Human Red Blood Cells with Tunable "Tug-of-War" Optical Tweezers, Phys. Rev. Appl. **12**, 064060 (2019).